IEEE Photonics Journal
An IEEE Photonics Society Publication

Mechanically Tunable Negative-Index Photonic Crystal Lens

Volume 2, Number 6, December 2010

Y. Cui
V. A. Tamma
J.-B. Lee
W. Park

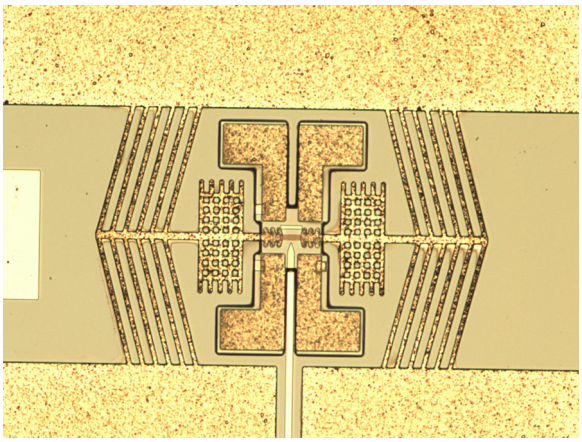

DOI: 10.1109/JPHOT.2010.2091116
1943-0655/$26.00 ©2010 IEEE

IEEE photonics SOCIETY

IEEE

Mechanically Tunable Negative-Index Photonic Crystal Lens

Y. Cui,[1,2] V. A. Tamma,[1] J.-B. Lee,[2] and W. Park[1]

[1]Department of Electrical, Computer and Energy Engineering, University of Colorado, Boulder, CO 80309-0425 USA
[2]Department of Electrical Engineering, University of Texas at Dallas, Richardson, TX 75080 USA

DOI: 10.1109/JPHOT.2010.2091116
1943-0655/$26.00 ©2010 IEEE

Manuscript received October 6, 2010; revised October 28, 2010; accepted October 30, 2010. Date of publication November 3, 2010; date of current version November 19, 2010. This work was supported in part by the National Science Foundation under Grant BES-0608934 and in part by the Army Research Office Multidisciplinary University Research Initiative under Contract 50432-PH-MUR. The work of Y. Cui was supported by the Jan P. Van Der Ziel Fellowship. Corresponding author: W. Park (e-mail: won.park@colorado.edu).

Abstract: We report the microelectromechanical systems (MEMS)-enabled mechanically tunable negative-index photonic crystal lens, which was comprised of 2-D photonic crystal and symmetrical electro-thermal actuators. The 2-D photonic crystal was made of a honeycomb lattice of silicon rods embedded in an SU-8 membrane. A silicon input waveguide and deflection block were also fabricated for light in-coupling and monitoring of focused spot size, respectively. When actuated, the electro-thermal actuators stretched the photonic crystal and consequently modified the photonic band structure. This, in turn, modified the focal length of the photonic crystal lens. The fabricated device was fully characterized using a tunable laser and an infrared camera while being actuated with a constant current source. The intensity and lateral spot size observed at the deflection block gradually increased as the applied current increased from 0 to 0.3 A. The observed behavior was in excellent agreement with finite-difference time-domain (FDTD) simulations, confirming the mechanical tuning of negative-index imaging.

Index Terms: Photonic crystals, Micro and Nano Opto-Electro-Mechanical Systems (MOEMS), Near field microscopy.

1. Introduction

Photonic crystals have attracted a great deal of research interest over the past two decades. [1], [2] Photonic crystals have demonstrated the capability of generating, manipulating, and detecting electromagnetic waves. [3] These artificially created crystals have been shown to exhibit many unique phenomena, some of which are not observable in natural materials. Examples include negative refraction [4]–[7], self-collimation [8]–[10], superprism [11], [12], strong light confinement [13], [14], and slow light [15]. While these unique features hold high promises for future photonics technology, most photonic crystal research has so far dealt with passive devices with no means of external control. Achieving dynamic tunability and on-demand control in photonic crystal devices would greatly expand their applications.

Since the optical properties of photonic crystal are essentially determined by the photonic band structure, achieving tunable photonic crystal means finding a way to modulate the photonic band structure. Generally, there are two main methods to realize tunable photonic crystals. One is to change the refractive index of the constituent materials, and the other is to change the lattice structure. Most of the tunable photonic crystals that have so far been reported incorporated refractive

index tuning with various means. Busch and John proposed tunable photonic band gap in an inverse opal structure infiltrated with nematic liquid crystal [16]. Roussey *et al.* utilized lithium niobate $(LiNbO_3)$ to realize electro-optically tunable photonic crystal [17], [18]. Schmidt *et al.* used polymethyl methacrylate (PMMA) and demonstrated an electro-optically tunable photonic crystal slab waveguide resonator [19]. These tunable photonic crystals were all based on electro-optic tuning of the refractive index. The thermo-optic effect was also used to achieve the tuning effect. Tinker *et al.* [20], [21] proposed the thermo-optic photonic crystal light modulator concept by thermo-optically tuning the photonic band structure to shift the cutoff wavelength by 60 nm near the telecommunication wavelength of 1550 nm. Cui *et al.* [22] also demonstrated focal length modulation in a photonic crystal lens by localized heating on the silicon photonic crystal region. However, with either electro-optic or thermo-optic tuning, the achievable tunability is limited due to the small attainable refractive index change [23].

As a radically different approach that could provide much greater tunability, Park and Lee proposed the mechanically tunable photonic crystal (MTPC) [24]. In an MTPC, mechanical actuators induce physical changes in the crystal structure to which photonic bands are highly sensitive. Although strain tuning of the silicon photonic crystal has been reported, [25] direct strain tuning of silicon and most other high-index materials is difficult due to their high Young's modulus. An inverted structure in which rods of high-Young's-modulus material are embedded in a membrane of low-Young's-modulus material can accommodate a much larger strain. The low-Young's-modulus membrane can easily be stretched by microactuators. It is therefore possible to introduce large deformation of lattice structure, leading to significant changes in the photonic band structure. Also, choosing a high-Young's-modulus material with high refractive index (e.g., Si, GaAs) and a low-Young's-modulus material with low refractive index [e.g., SU-8, Polydimethylsiloxane (PDMS)] provides a large index contrast, which is often needed for novel optical phenomena.

2. Device Design and Fabrication

While the MTPC may be used for a variety of optical devices such as tunable filters, resonators, and waveguides, in this paper, we demonstrate mechanical tuning of negative-index imaging. Although a cavity with sharp resonance would have been easier to demonstrate tunability, a strongly frequency-dispersive lens could enable novel applications such as a lab-on-a-chip biosensor. Fig. 1(a) shows the schematic overview of the entire device. Fig. 1(b) shows a close-up view of the SU-8 membrane in which a photonic crystal lens, a silicon input waveguide tip, a deflection block, and joints to the actuators are embedded. For the negative-index photonic crystal structure, a honeycomb lattice of silicon nanorods was chosen. The simple hexagonal array of rods or holes is the more commonly used structure. While the simple hexagonal lattice also exhibits negative refraction in the second photonic band, the third photonic band overlaps the second band, leading to beam splitting. In the honeycomb lattice, the introduction of two atom basis breaks the symmetry and lifts the degeneracy between the second and third bands [26]. Our photonic crystal lens consisted of 7×28 hexagonal units of silicon rods embedded in SU-8 and was oriented in such a way that Γ–M direction was along the optic axis. For mechanical tuning, the silicon nanorod array was embedded in an SU-8 membrane, and the whole structure was air-suspended. To maintain structural stability, the SU-8 layer was made to be 10 μm thick, and thus, the MTPC structure can be regarded as a slab photonic crystal with SU-8 upper cladding and air lower cladding. The thick SU-8 upper cladding prevented the direct imaging of the near field, and thus, the MTPC was designed to be characterized by capturing the out-of-plane scattered light in the far field. In order to facilitate the far-field measurements, a deflection block was placed 9 μm behind the photonic crystal. This negative-index lens had a numerical aperture of 0.48 and an image distance of 7 μm at the wavelength of 1600 nm. Detailed analysis of how the lens performance changes with mechanical tuning has been published elsewhere [26], [27].

For mechanical tuning, a pair of electro-thermal actuators was attached symmetrically on both sides of the SU-8 membrane, as shown in Fig. 1(a) and (b). Both the actuators and the SU-8 membrane were suspended in air with the support from four anchors at the electrical pads of the

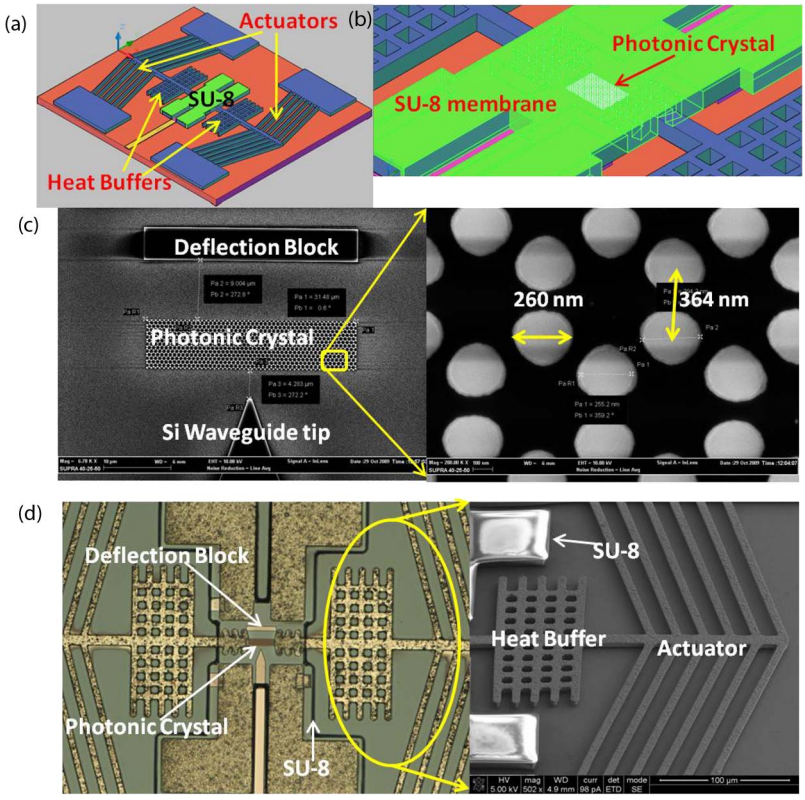

Fig. 1. (a) Schematic diagram showing mechanically tunable photonic crystal. (b) Close-up view of the SU-8 membrane, which has an array of silicon rods (photonic crystal) embedded in. (c) SEM images of tapered silicon waveguide, photonic crystal, and deflection block, as well as a close-up view of the silicon rods in a honeycomb lattice. (d) Optical and SEM images of mechanically tunable photonic crystal lens.

actuators. The chevron-shape microactuators were designed to be powerful and stable enough to stretch and support the SU-8 membrane, thereby inducing the required lattice structure change without unwanted deformation. Once actuated, the actuators would stretch the SU-8 membrane from both sides, leading to uniaxial elongation of photonic crystal lattice in the direction perpendicular to the light propagation. Since Young's modulus of SU-8 is in the range of 1 $\sim$ 4 GPa [28], [29] and the mechanical force generated by MEMS actuators is typically in the range of a few millinewtons, the SU-8 membrane can be stretched up to a few percentage strain, which is many orders of magnitude greater in that which is achievable in high-Young's-modulus materials such as Si. The maximum tuning capability of the MTPC system is decided by the elastic limit of the cross-linked SU-8, which is 2 $\sim$ 3% [30]. In order to ensure that the actuators were powerful enough to demonstrate mechanical tuning of the photonic crystal lens, chevron-shape nickel actuators were designed by the finite element method (FEM). Each actuator was comprised of six pairs of nickel beams. Each beam was 5 μm wide, 5 μm thick, and 200 μm long with 15° angle to the central axis of the actuator. Two identical actuators were placed 30 μm apart so that they would pull the MTPC membrane from both sides. After oxide release, all the actuators and the photonic crystal membrane were freely suspended at 2 μm above the substrate. For actuation, a current was supplied to the nickel actuators, leading to joule heating of the nickel beams. The resulting thermal expansion of the nickel beams then stretched the MTPC membrane. The response time of this kind of nickel actuator is expected to be of the order of milliseconds [31], [32]. Therefore, the maximum operating frequency of the system should be a few kilohertz. Power consumption varies with the strain and was found to be 35 mW to maintain a strain of 1.4%, which was the maximum strain used in this work. During the

actuator operation, maintaining strain with good control could be an issue. In order to achieve good control, the actuator temperature must stabilize quickly. Since the major heat-dissipation channel is through the air gap and into the substrate, increasing the thermal conductivity of the air gap could lead to fast temperature stabilization. The simplest way to achieve this is to increase the air pressure. Alternatively, the air medium could be replaced by a high thermal conductivity, low dynamic viscosity gas such as Helium.

Fabrication of the MTPC started with photolithography of the silicon waveguide and electron beam lithography of the silicon rod array on the silicon-on-insulator (SOI) wafer. The silicon input waveguide and alignment marks were patterned by photolithography, and the pattern was transferred to 100-nm chromium layer by the evaporation and lift-off processes. Subsequently, copolymer resist and PMMA e-beam resist were coated on top of the SOI wafer and patterned by electron beam lithography to form photonic crystal lens, the tapered tip of the waveguide, and the deflection block. A 20-nm thick chromium layer was evaporated and pattern transferred by a lift-off process. By using 100-nm and 20-nm chromium layers as a protective mask, a 340-nm-thick top silicon was dry etched by reactive ion etch (RIE) with CF_4/O_2 (91.25%: 8.75%) plasma. Then, chevron-shape electro-thermal actuator fabrication was started. Electro-plating seed layers of chromium and copper were deposited by evaporation. SPR 220 positive photoresist was used to form the chevron actuator mold with an 11-μm trench depth by photolithography. The 5-μm-thick nickel was electroplated to form symmetrical electro-thermal six-beam chevron actuators. A 10-μm-thick SU-8 was subsequently spin-coated and patterned to selectively cover a silicon rod array, a deflection block, the tip of the tapered input waveguide, the joint part of the chevron actuators, and nickel anchors to form a mechanically tunable photonic crystal. Finally, the oxide underneath the SU-8 membrane and chevron actuators was selectively etched away, resulting in an air-suspended photonic crystal lens and actuators. Gold wire-bonding technology was used to couple the electric power into the tiny nickel pads of a mechanically tunable photonic crystal. Gold wires were connected from the tiny pads of nickel actuators to macroscopic gold pads which were prefabricated on a glass slide. The macroscopic gold pads were connected to the power source through soldered metal wires. Fig. 1(c) shows the scanning electron microscope (SEM) images of the fabricated tapered waveguide, photonic crystal, and deflection block, as well as a close-up view of the silicon rods before SU-8 coating. Fig. 1(d) shows the optical micrograph of chevron actuator integrated with MTPC, an input waveguide, and a deflection block.

Fig. 1(d) also shows heat buffers and nickel anchors. In order to prevent misalignment between the tapered silicon input waveguide, the photonic crystal lens, and the deflection block, it was critical to minimize any out-of-plane bending of the photonic crystal membrane during actuation. For this purpose, four nickel anchors were embedded at the four corners of the photonic crystal membrane, as shown in Fig. 1(d). The anchors were firmly attached to the substrate via buried oxide layer, thereby providing strongholds for the photonic crystal membrane and consequently minimizing vertical movement. On the other hand, two heat buffers were placed between the actuators and photonic crystal membrane to suppress the heat conduction from the actuator to the photonic crystal membrane. The heat buffer had a grid-like shape so that the large surface area effectively dissipated the heat and prevented the temperature from rising in the photonic crystal region. This was necessary to eliminate the possibility of photonic crystal tuning by the thermo-optic effect. Fig. 2(a) shows the finite element analysis result of the heat buffer and chevron actuator, and Fig. 2(b) shows the temperature profile along the central axis of the chevron actuator to the SU-8 membrane during mechanical actuation. It was found that the temperature varied slowly in the shuttle region of the actuator, while it dropped rapidly in the heat-buffer region, resulting in little temperature change in the photonic crystal region during actuation. Due to the many components needed in the whole system, the fabrication process consisted of many carefully designed steps, and some details of the fabrication processes have been reported in previous publications [33], [34].

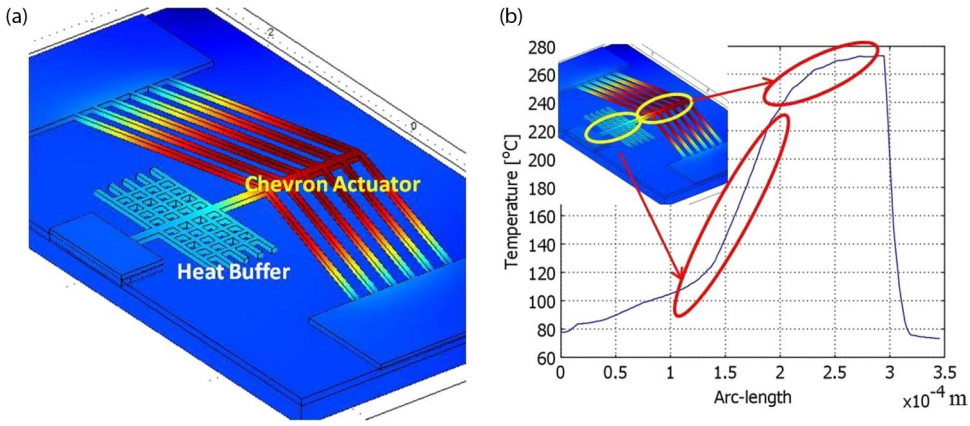

Fig. 2. (a) Schematic diagram showing chevron-shape nickel actuator and heat-buffer. (b) Temperature profile along the central axis of the actuator and SU-8 membrane.

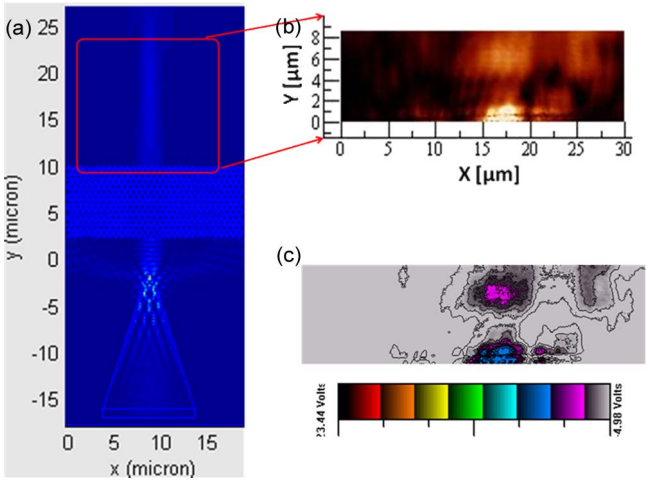

Fig. 3. (a) Two-dimensional FDTD simulation result of photonic crystal lens with tapered waveguide at the wavelength of 1.6 μm. (b) NSOM scanned image of photonic crystal edge and focal point area. (c) Light intensity contour of the NSOM image.

3. Optical Characterizations

The focusing characteristics of the photonic crystal were first investigated by near-field scanning optical microscopy (NSOM). As described before, the actual MTPC sample had a 10-μm-thick SU-8 upper cladding for mechanical stability, and this made it impossible to obtain near-field images of the light propagating through the photonic crystal layer. We therefore fabricated separate samples for NSOM measurements by coating a thin layer of SU-8 (500 nm) over the silicon nanorod array and not etching the 2-μm-thick buried oxide. Since the refractive indexes of silicon dioxide and SU-8 are similar, this structure may be considered identical to the air-suspended MTPC with a thick SU-8 overlayer, except that the structure is upside down. The NSOM scan was then performed over the SU-8 surface. In these experiments, three fiber-coupled lasers tunable between 1400 and 1602 nm were used as a light source. A polarization controlling paddle was used to set the correct polarization of the laser, and the light output from the fiber was butt-coupled into the input waveguide. The NSOM scanning process consisted of three steps. First, the tip oscillation amplitude and phase were set. Then, the desired scan area was established via a topology scan. Finally, the near-field optical image was obtained by scanning the area again with light input.

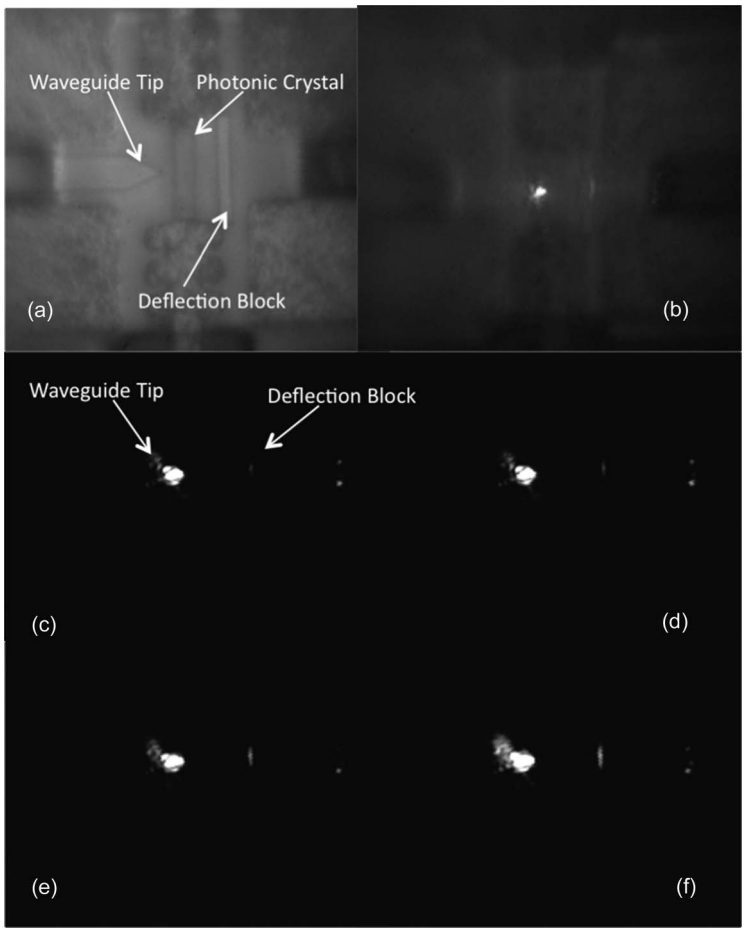

Fig. 4. (a) Optical image of MTPC before far-field imaging. (b) Optical image with infrared light coupled in the waveguide. Infrared CCD camera images taken at the wavelength of 1465 nm with transverse magnetic polarization at applied current of (c) 0 A, (d) 0.1 A, (e) 0.2 A, and (f) 0.3 A.

Fig. 3(a) shows a 2-D finite difference time domain (FDTD) simulation result of the photonic crystal structure with a tapered tip input silicon waveguide at 1.6-μm wavelength. As shown, the tapered waveguide tip mimicked a point source, producing a diverging incident field. The photonic crystal lens then focused the diverging light from the waveguide tip to a single focal point which was placed approximately 7 μm away from the rear edge of the photonic crystal lens. Fig. 3(b) shows the NSOM image over a region spanning from the rear edge of the photonic crystal to the focal point. A bright light spot was observed at the rear edge of the photonic crystal lens due to strong light scattering expected at the interface between the photonic crystal structure and SU-8. Another fainter yet clearly identifiable spot was observed approximately 7 μm away from the rear edge of the photonic crystal, directly demonstrating negative-index imaging. The position of the focal point was in excellent agreement with the FDTD simulation in Fig. 3(a). The focused spot was seen much more prominently in the intensity contour plot of NSOM image shown in Fig. 3(c). The NSOM results confirmed that the fabricated photonic crystal indeed exhibited negative index and that the focusing characteristics agreed well with the numerical simulations.

To directly observe mechanical tuning, the light scattered off the deflection block was imaged in the far field, while constant current was applied to the actuators to induce mechanical stretching in the MTPC structure. In the far-field measurements, laser sources and input coupling conditions were identical to the near-field measurements. The out-of-plane scattered light from the input waveguide, PC, and deflection block regions was collected by an objective lens and imaged onto an

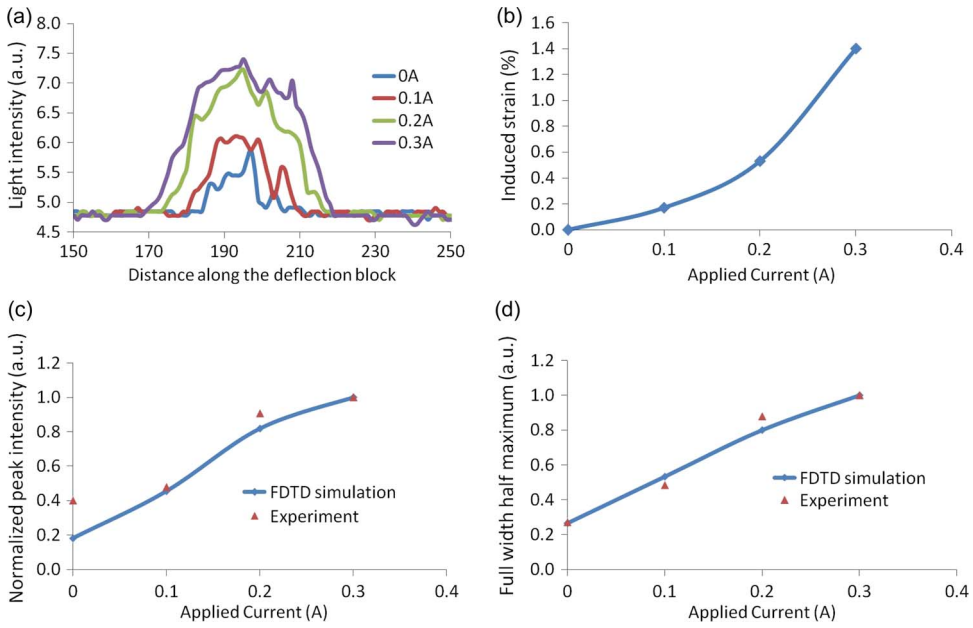

Fig. 5. (a) Experimentally measured light intensity profile of the light spot at the deflection block with various applied currents. (b) COMSOL simulated strain as a function of applied current. (c) Experimental and 2-D FDTD simulated results of the peak light intensity at the deflection block as a function of applied current. (d) Experimental and 2-D FDTD simulated results of the light spot size (FWHM) at the deflection block as a function of applied current.

infrared vidicon camera which recorded the intensity of scattered light from different interfaces. Further, a Tungsten lamp was used with the above setup to obtain images of the different regions and interfaces under measurement. Fig. 4(a) and (b) show the optical micrographs of MTPC before and after the laser beam is coupled into the input waveguide. Scattered light spots were observed at the tapered input waveguide tip and deflection block. Fig. 4(c)–(f) show the infrared images of the waveguide tip and deflection block with applied currents of 0, 0.1, 0.2, and 0.3 A at the wavelength of 1465 nm with transverse magnetic polarization. A bright light spot was captured in the input waveguide tip region, while a slightly weaker spot was also observed at the deflection block. For detailed analysis, the far-field images were digitized, and the intensity profiles at the deflection block were extracted. The extracted intensity profiles along the edge of the deflection block are plotted in Fig. 5(a). As shown, both the peak intensity and the spot width increased, as the applied current was increased. The interference fringes superimposed over the intensity profiles were due to the reflections from the nickel actuators.

To properly analyze the tuning results, we must first know the extent of stretching under various applied currents. The mechanical actuation of MTPC was directly measured by SEM, and mechanical strain of up to $\Delta l/l_o = 7\%$ was observed, where Δl is the stretched length, and l_o is the unstretched dimension [35]. However, the heat dissipation from the nickel actuators in the vacuum environment of the SEM chamber should be different from that in the atmosphere in which the optical measurements were carried out. Since it was not possible to directly measure the submicrometer scale actuation distance in air, finite element simulation (COMSOL) was used to estimate the displacement of the actuator and induced strain $(\Delta l/l_o)$ as a function of applied current. In order to simulate the actuator operation accurately, the actuator model was built based strictly on the measured nickel beam dimensions and measured nickel resistivity. The thicknesses of nickel and the SU-8 membrane were measured to be 5 and 10 μm, respectively. In order to estimate the nickel resistivity, the resistance of a virgin chevron actuator with identical dimensions was measured before and after actuation by the four-point probe method. Upon actuation, the actuator resistance increased due most likely to thermal oxidation and electromigration induced by

heat and large current density, respectively. After several actuations, the resistance stabilized to a steady value. The measured increase in resistance allows us to calculate the increase in resistivity. The final nickel resistivity in our actuators during operation was determined to be 7.4×10^{-7} Ωm. Using the nickel beam dimensions and resistivity, the strain induced by the nickel actuator as a function of applied current was calculated by COMSOL. As shown in Fig. 5(b), the induced strains under applied currents of 0, 0.1, 0.2, and 0.3 A were estimated to be 0%, 0.17%, 0.53%, and 1.4%, respectively. Due to the slight increase in nickel resistivity during the initial actuations, the MTPC underwent reasonably large, stretching at low applied currents. The induced strains were, however, lower than those in a vacuum because of the higher heat dissipation in air, which would consequently lead to lower temperature and, thus, smaller thermal expansion.

Another important consideration was the fact that the SU-8 membrane shrinks when released from the silicon dioxide substrate. The shrinkage is caused by preexisting surface tension between SU-8 and silicon dioxide as well as the internal stress of SU-8 developed during the curing process. Consequently, the SU-8 membrane tends to shrink after oxide release. The shrinkage was first directly measured by cutting the membrane with focused ion beam and imaging the cross-section with SEM. By comparing with the SEM images of the silicon nanorod array taken before SU-8 deposition, shrinkage was estimated to be 4.8% [35]. For the current device employing a 10-μm-thick SU-8 membrane, the shrinkage was estimated by comparing FEM simulations, FDTD simulations, and experiment results because nondestructive, direct measurements were not possible. The initial SU-8 membrane shrinkage estimated this way was 7.7%. The internal stress of SU-8 is strongly related to the temperature change in the curing process. During the 10-μm SU-8 curing process, the temperature change was relatively aggressive, and we suspect that this induced large internal stress in the SU-8 membrane, resulting in somewhat larger shrinkage than the previous device.

Using the induced strain calculated by COMSOL and taking into account the initial SU-8 shrinkage, FDTD simulations were conducted to obtain the intensity profile at the position of the deflection block. Also, to properly compare the simulated intensity profile with the experimental results, the infrared camera response was carefully calibrated against the laser power. As reported previously [26], the simulation showed that the focal point moved away from the photonic crystal lens as the MTPC was stretched. The intensity profiles extracted from the simulation results were then compared with the experimental results given in Fig. 5(a). The calculated peak light intensities at the deflection block were 0.017, 0.02, 0.024, and 0.026 (a.u.) for 0%, 0.17%, 0.53%, and 1.4% stretching, respectively. The peak intensity at the deflection block increased as the MTPC was stretched, as observed in the experiments. Fig. 5(c) shows experimental and simulation results of relative peak light intensity at the deflection block as a function of applied current. The relative peak intensities were obtained by normalizing with respect to the maximum peak intensity obtained at 1.4% stretching. It is clear that the experiments and simulations agree very well. Experimental and simulated full-width at half-maximum (FWHM) at the deflection block were also compared. Fig. 5(d) shows the normalized FWHM as a function of applied current for both experimental and 2-D FDTD simulation results. Once again, the experimental and simulation results agree with each other very well. The excellent agreement between experiments and simulation indicate that the experimentally observed changes in intensities and widths were indeed due to the mechanical tuning of negative refraction in MTPC.

4. Conclusion

In conclusion, mechanically tunable negative-index photonic crystal lens was designed, fabricated, and experimentally demonstrated. The photonic crystal structure was composed of silicon nanorods embedded in an SU-8 membrane and designed to exhibit negative refraction near the wavelength of 1.5 μm. Mechanical stress was applied by a pair of nickel electro-thermal actuators. Mechanical stretching of photonic crystal membrane induced significant change in the photonic crystal band structure, leading to shifts in focal length. By monitoring the light scattering off the deflection block, the shift in focal length was directly visualized. The experimentally observed peak intensity and FWHM were in excellent agreement with FDTD simulations, confirming the successful mechanical

tuning of negative-index imaging. The tunable negative-index microlens demonstrated in this paper opens doors to a wide range of novel applications such as the integrated optical sensor, micro-spectrometer, and adaptive optical system.

References

[1] E. Yablonovitch, "Inhibited spontaneous emission in solid-state physics and electronics," *Phys. Rev. Lett.*, vol. 58, no. 20, pp. 2059–2062, May 1987.

[2] S. John, "Strong localization of photons in certain disordered dielectric superlattices," *Phys. Rev. Lett.*, vol. 58, no. 23, pp. 2486–2489, Jun. 1987.

[3] J. D. Joannopoulos, S. G. Johnson, J. N. Winn, and R. D. Meade, *Photonic Crystals: Molding the Flow of Light,* 2nd ed. Princeton, NJ: Princeton Univ. Press, 2008.

[4] M. Notomi, "Theory of light propagation in strongly modulated photonic crystals: Refractionlike behavior in the vicinity of the photonic band gap," *Phys. Rev. B, Condens. Matter Mater. Phys.*, vol. 62, no. 16, pp. 10 696–10 705, Oct. 2000.

[5] E. Schonbrun, Q. Wu, W. Park, T. Yamashita, C. J. Summers, M. Abashin, and Y. Fainman, "Wave front evolution of negatively refracted waves in photonic crystals," *Appl. Phys. Lett.*, vol. 90, no. 4, p. 041113, Jan. 2007.

[6] P. V. Parimi, W. T. Lu, P. Vodo, and S. Sridhar, "Photonic crystals: Imaging by flat lens using negative refraction," *Nature*, vol. 426, no. 6965, p. 404, Nov. 2003.

[7] E. Schonbrun, T. Yamashita, W. Park, and C. J. Summers, "Negative-index imaging by an index-matched photonic crystal slab," *Phys. Rev. B, Condens. Matter Mater. Phys.*, vol. 73, no. 19, p. 195117, May 2006.

[8] P. T. Rakich, M. S. Dahlem, S. Tandon, M. Ibanescu, M. Soljacic, G. S. Petrich, J. D. Joannopoulos, L. A. Kolodziejski, and E. P. Ippen, "Achieving centimet re-scale supercollimation in a large-area two-dimensional photonic crystal," *Nat. Mater.*, vol. 5, no. 2, pp. 93–96, Feb. 2006.

[9] E. Schonbrun, Q. Wu, W. Park, T. Yamashita, and C. J. Summers, "Polarization beam splitter based on a photonic crystal heterostructure," *Opt. Lett.*, vol. 31, no. 21, pp. 3104–3106, Oct. 2006.

[10] W. Park, "Controlling the flow of light with silicon nanostructures," *Laser Phys. Lett.*, vol. 7, no. 2, pp. 93–103, Jan. 2010.

[11] H. Kosaka, T. Kawashima, A. Tomita, M. Notomi, T. Tamamura, T. Sato, and S. Kawakami, "Superprism phenomena in photonic crystals," *Phys. Rev. B, Condens. Matter Mater. Phys.*, vol. 58, no. 16, pp. R10096–R10099, Oct. 1998.

[12] W. Park and C. J. Summers, "Extraordinary refraction and dispersion in 2D photonic crystal slabs," *Opt. Lett.*, vol. 27, no. 16, pp. 1387–1389, Aug. 2002.

[13] Y. Akahane, T. Asano, B.-S. Song, and S. Noda, "Hight-Q photonic nanocavity in a two-dimensional photonic crystal," *Nature*, vol. 425, no. 6961, pp. 944–947, Oct. 2003.

[14] B.-S. Song, S. Noda, T. Asano, and Y. Akahane, "Ultra-high-Q photonic double-heterostructure nanocavity," *Nat. Mater.*, vol. 4, no. 3, pp. 207–210, Mar. 2005.

[15] T. Baba, "Slow light in photonic crystals," *Nat. Photon.*, vol. 2, no. 8, pp. 465–473, Aug. 2008.

[16] K. Busch and S. John, "Liquid-crystal photonic-band-gap materials: The tunable electromagnetic vacuum," *Phys. Rev. Lett.*, vol. 83, no. 5, pp. 967–970, Aug. 1999.

[17] M. Roussey, M. P. Bernal, N. Courjal, and F. I. Baida, "Experimental and theoretical characterization of a lithium niobate photonic crystal," *Appl. Phys. Lett.*, vol. 87, no. 24, p. 241101, Dec. 2005.

[18] M. Roussey, M. P. Bernal, N. Courjal, D. V. Labeke, F. I. Baida, and R. Salut, "Electro-optic effect exaltation on lithium niobate photonic crystals due to slow photons," *Appl. Phys. Lett.*, vol. 89, no. 24, p. 241110, Dec. 2006.

[19] M. Schmidt, M. Eich, U. Huebner, and R. Boucher, "Electro-optically tunable photonic crystals," *Appl. Phys. Lett.*, vol. 87, no. 12, p. 121110, Sep. 2005.

[20] M. Tinker and J.-B. Lee, "Thermal and optical simulation of a photonic crystal light modulator based on the thermo-optic shift of the cut-off frequency," *Opt. Express*, vol. 13, no. 18, pp. 7174–7188, Sep. 2005.

[21] M. Tinker and J.-B. Lee, "Thermo-optic photonic crystal light modulator," *Appl. Phys. Lett.*, vol. 86, no. 22, p. 221111, May 2005.

[22] Y. Cui, K. Liu, S. Foland, K. H. Choi, M. Tinker, D. MacFarlane, and J.-B. Lee, "Silicon-based thermo-optically tunable photonic crystal lens," *IEEE Photon. Technol. Lett.*, vol. 22, no. 1, pp. 21–23, Jan. 2010.

[23] C. J. Summers, C. W. Neff, and W. Park, "Active photonic crystal nano-architectures," *J. Nonlinear Opt. Phys. Mater.*, vol. 12, no. 4, pp. 587–597, Dec. 2003.

[24] W. Park and J.-B. Lee, "Mechanically tunable photonic crystal structure," *Appl. Phys. Lett.*, vol. 85, no. 21, pp. 4845–4847, Aug. 2004.

[25] C. W. Wong, P. T. Rakich, S. G. Johnson, M. Qi, H. I. Smith, E. P. Ippen, L. C. Kimerling, Y. Jeon, G. Barbastathis, and S.-G. Kim, "Strain-tunable photonic band gap microcavities in optical waveguides," *Appl. Phys. Lett.*, vol. 84, no. 8, pp. 1242–1244, Feb. 2004.

[26] Q. Wu, E. Schonbrun, and W. Park, "Tunable superlensing by a mechanically controlled photonic crystal," *J. Opt. Soc. Amer. B, Opt. Phys.*, vol. 23, no. 3, pp. 479–484, Mar. 2006.

[27] Q. Wu and W. Park, "Broadband sub-wavelength imaging by mechanically tunable photonic crystal," *J. Comput. Theor. Nanosci.*, vol. 2, no. 2, pp. 202–206, Jun. 2005.

[28] H. Lorenz, M. Despont, N. Fahrni, N. Labianca, P. Renaud, and P. Vettiger, "SU-8: A low-cost negative resist for MEMS," *J. Micromech. Microeng.*, vol. 7, no. 3, pp. 121–124, Apr. 1997.

[29] S. F. Hwang, J. H. Yu, B. J. Lai, and H. K. Liu, "Young's modulus and interlaminar fracture toughness of SU-8 film on silicon wafer," *Mech. Mater.*, vol. 40, no. 8, pp. 658–664, Feb. 2008.

[30] S. Singamaneni, K. Bertoldi, S. Chang, J. Jang, E. L. Thomas, M. C. Boyce, and V. V. Tsukruk, "Instabilities and pattern transformation in periodic, porous elastoplastic solid coatings," *Appl. Mater. Interfaces*, vol. 1, no. 1, pp. 42–47, Jan. 2009.

[31] E. T. Enikov and K. Lazarov, "PCB-integrated metallic thermal micro-actuators," *Sens. Actuators A, Phys.*, vol. 105, no. 1, pp. 76–82, Jun. 2003.
[32] A. A. Geisberger and N. Sarkar, "Techniques in MEMS microthermal actuators and their applications," in *Proc. MEMS/NEMS*, 2006, pp. 201–261.
[33] M. Tinker, E. Schonbrun, J.-B. Lee, and W. Park, "Process integration and development of inverted photonic crystal arrays," *J. Vac. Sci. Technol. B, Microelectron. Nanometer Struct.*, vol. 24, no. 2, pp. 705–709, Mar. 2006.
[34] E. Schonbrun, M. Tinker, W. Park, and J.-B. Lee, "Negative refraction in a Si-polymer photonic crystal membrane," *IEEE Photon. Technol. Lett.*, vol. 17, no. 6, pp. 1196–1198, Jun. 2005.
[35] Y. Cui, Q. Wu, W. Park, J. Jeon, M. J. Kim, and J.-B. Lee, "MEMS based mechanically tunable flexible photonic crystal," in *Proc. Transducers*, 2009, pp. 509–512.